sustainability

MDPI

Article

Biomass-Derived Carbon–Silica Hybrid Biochar for Nano- and Microplastic Adsorption

Weimin Gao [1,2], Qiyang Ling [1,2,*], Dantong Zhu [1,2] and Xiangju Cheng [1,2]

[1] School of Civil Engineering & Transportation, South China University of Technology, Guangzhou 510640, China; gaoweimin0823@outlook.com (W.G.); chengxiangju@scut.edu.cn (X.C.)
[2] State Key Laboratory of Subtropical Building and Urban Science, South China University of Technology, Guangzhou 510640, China
* Correspondence: lingqy@scut.edu.cn

Abstract

Nano- and microplastic contamination poses a growing challenge to aquatic environments, driving the need for efficient and sustainable removal technologies. In this study, carbon–silica hybrid nanoparticles (CSNPs) were synthesized from rice husk-derived black liquor via controlled lignin–silica self-assembly followed by thermal carbonization, providing a waste-recycling biorefinery route for value-added material production. Structural characterizations revealed that carbonization generates a hierarchically porous carbon–silica hybrid with enhanced surface area. The CSNPs exhibited rapid and size-dependent adsorption toward nano- and microplastics (200–1000 nm), with optimal performance observed for 500 nm particles. Microscopic observations further demonstrated a size-adaptive capture mechanism, involving pore filling and surface adsorption for nanoplastics and aggregate-assisted encapsulation for larger microplastics. This study highlights CSNPs as low-cost and effective adsorbents for broad-spectrum plastic removal while offering a sustainable pathway for the high-value utilization of black liquor and rice husk biomass in water purification applications.

Keywords: biochar; carbon material; nano- and microplastic; black liquor; biosilica

1. Introduction

Water pollution resulting from anthropogenic activities has become a critical environmental and public health challenge [1]. The widespread presence of persistent contaminants, including plastics, heavy metals, and organic dyes, in aquatic systems poses severe threats to ecological integrity and the security of drinking water supplies [2]. In particular, the global accumulation of plastic waste originates from the fragmentation of larger plastic debris and direct emissions from industrial and domestic sources, attracting increasing concern due to its environmental persistence and long-term ecological impacts [3]. Nano- and microplastics (NMPs), owing to their small particle size, heterogeneous surface properties, and high environmental persistence, exhibit complex transport and accumulation behaviors in aquatic environments [4]. These properties, combined with their resistance to degradation, render nano- and microplastic (NMPs) particularly difficult to remove using conventional water treatment technologies [5]. The economic implications of this crisis are substantial: recent estimates suggest that plastic pollution contributes to global health-related economic losses exceeding $1.5 trillion annually [6], while the global market for microplastic removal technologies is projected to reach $3.77 billion by 2033, growing

Check for updates

Academic Editor: Francesco Nocera

Received: 11 March 2026
Revised: 28 March 2026
Accepted: 2 April 2026
Published: 9 April 2026

Copyright: © 2026 by the authors. Licensee MDPI, Basel, Switzerland. This article is an open access article distributed under the terms and conditions of the Creative Commons Attribution (CC BY) license.

at a compound annual rate of 13.2% [7]. Their widespread occurrence in natural water bodies highlights the urgent need to develop efficient, sustainable, and cost-effective water purification strategies.

Among currently available water treatment technologies, including membrane separation, advanced oxidation, and electrochemical processes, adsorption has emerged as a particularly attractive option because of its operational simplicity, scalability, and cost-effectiveness [8]. It generates minimal secondary pollution and enables straightforward regeneration and reuse of adsorbents [9]. Conventional adsorbents, such as activated carbon, metal oxides, and zeolites, generally exhibit high adsorption capacities [10]. Nevertheless, their widespread application is often constrained by high production costs and reliance on non-renewable resources [11]. Consequently, increasing attention has been directed toward the development of low-cost, renewable, and sustainable alternatives, with biomass-derived adsorbents emerging as promising candidates for large-scale and environmentally sustainable water purification applications [12].

Agricultural residues such as rice husk, sugarcane bagasse, and fruit peels have been widely investigated as low-cost precursors for carbonaceous materials due to their high-carbon content and intrinsic mineral composition [13]. Rice husk, generated in large quantities as an agricultural by-product, exhibits a distinctive compositional architecture in which lignocellulosic lignin matrices are intrinsically integrated with a substantial silica fraction [14–16]. Lignin is the most abundant renewable aromatic biopolymer in nature and is an integral structural component of lignocellulosic biomass [17]. Despite its high carbon content and rich aromatic framework, lignin has historically been treated as a low-value byproduct of the pulping and paper-making industries. Approximately 100 million tons of lignin are generated annually from industrial pulping processes, while the majority is combusted for low-grade energy recovery, and only a small fraction is recovered from pulping black liquor for the production of value-added materials [18,19]. When derived from rice husk, lignin is inherently coupled with silica-rich mineral phases, creating an organic–inorganic architecture that is particularly advantageous for constructing hybrid adsorbents with enhanced structural stability and high adsorption capacity [20]. Such architectures enhance mass transfer dynamics, maximize the exposure of adsorption-active sites, and enable multiple interaction mechanisms with contaminants of diverse physicochemical properties [21]. The conversion of rice husk into functional adsorbents constitutes a resource-efficient valorization pathway that transforms an abundant agricultural by-product into high-performance materials, supporting sustainable materials development while reducing reliance on synthetic adsorbents for water purification applications [22].

Carbon- and silica-based materials have been widely explored as effective adsorbents for water treatment applications. Carbonaceous adsorbents, including activated carbon and biochar, are characterized by high porosity, large specific surface area, and chemically diverse functional groups, which collectively enable hydrophobic interactions, electrostatic attraction, and π–π interactions with organic contaminants [23]. In contrast, silica-based adsorbents exhibit a high density of surface hydroxyl groups, pronounced structural stability, and strong affinity for polar and charged species [24]. Carbon–silica hybrid nanoparticles combine the complementary attributes of these two material classes, addressing the intrinsic limitations associated with single-component adsorbents [25]. This synergistic integration gives rise to multifunctional hybrid nanomaterials with enhanced robustness and broad adsorption versatility. As a result, carbon–silica hybrids represent a promising class of advanced adsorbents for addressing complex and emerging water pollution challenges, including the removal of nanoplastics from aqueous systems. In this context, industrial black liquor generated from rice husk pulping represents a particularly promising feedstock. Traditionally regarded as a challenging waste stream, black liquor is

rich in lignin fragments, dissolved polysaccharides, and silica species. Leveraging these intrinsic components, lignin–silica nanoparticles (LSNPs) can be synthesized through controlled self-assembly. Subsequent carbonization of LSNPs yields carbon–silica nanoparticles (CSNPs) with enhanced porosity, stability, and surface activity. This two-step strategy not only valorizes an abundant waste stream but also enables the design of advanced hybrid nanomaterials tailored for pollutant adsorption. Notably, unlike previous studies that utilize only the organic or inorganic fraction of rice husk separately, our approach simultaneously valorizes both lignin and silica from black liquor through a one-pot self-assembly process without external reagents or templates. Furthermore, to the best of our knowledge, this is the first study to systematically evaluate such biomass-derived carbon–silica hybrids for the adsorptive removal of plastics across a wide size range—from nanoplastics to microplastics. This work presents the first demonstration of rice husk-derived carbon–silica hybrids for simultaneous nano- and microplastic removal, establishing a new valorization route for black liquor waste. The present study reports the synthesis of CSNPs from rice husk biomass-derived black liquor through an integrated LSNPs self-assembly and carbonization process. The prepared CSNPs were systematically characterized to assess their morphology, porosity, and surface chemistry, and their performance was evaluated for the adsorption of nanoplastics from aqueous solutions. This work highlights both a novel pathway for sustainable utilization of black liquor and the application of carbon–silica hybrid nanoparticles as efficient, low-cost, and environmentally benign adsorbents for next-generation water purification.

2. Materials and Methods

2.1. Materials

Rice husks (RH) were milled in a cutting mill and passed through a 0.25 mm sieve. Sodium hydroxide (NaOH) pellets, sulfuric acid H_2SO_4 (98%), and PEG-2000 were purchased from Aladdin Biochemical Technology Co., Ltd., Shanghai, China.

2.2. Rice Husk Pretreatment

Rice husk pretreatment was performed following our previously reported procedure [26]. Briefly, milled rice husk (30 g) was mixed with 150 g of a 3% (*w*/*w*) NaOH solution in a 200 mL sealed reactor and heated at 170 °C for 1 h. After pretreatment, the resulting solid residue and alkaline hydrolysate (black liquor, pH ≈ 13.2) were separated by vacuum filtration using filter paper.

2.3. Preparation of Lignin–Silica Nanoparticles

LSNPs were prepared by mixing 100 mL of black liquor with 50 mL of ultrapure water and 50 mL of ethanol, followed by the addition of 2 g PEG-2000. Under magnetic stirring at room temperature, 1 M H_2SO_4 was added dropwise until the pH reached 5. The mixture was then allowed to stand for 30 min to facilitate the assembly of lignin–silica particles. Finally, the LSNPs were collected by vacuum-assisted filtration, washed with water to neutral pH, and freeze-dried.

2.4. Formation of Carbon–Silica Nanoparticles

The dried lignin–silica nanoparticles (LSNPs) were subjected to thermal carbonization in a tubular furnace (BEQ Instrument Co., Ltd., Tianjin, China) under an inert atmosphere. Prior to heating, the furnace chamber was purged with high-purity nitrogen (99.999%) at a flow rate of 100 mL min^{-1} for 10 min to eliminate residual oxygen. The samples were loaded into a ceramic boat and placed in the central heating zone of the tube furnace. The samples were heated from room temperature to the designated terminal temperatures of

500 °C at a constant heating rate of 5 °C min^{-1} under continuous nitrogen flow. Each target temperature was maintained for 2 h to ensure adequate carbonization while preserving the integrity of the carbon and silica domains. Following treatment, the furnace was allowed to cool naturally to room temperature under nitrogen protection. The resulting carbon–silica hybrid nanoparticles were collected and denoted as CSNPs.

2.5. Analysis of Rice Husk-Derived Carbon/Silica Nanoparticles

2.5.1. Morphology

The morphological characteristics of the LSNPs and CSNPs were examined using scanning electron microscopy (SEM). For SEM analysis, the samples were dispersed in deionized water at a concentration of 1 wt.% and homogenized by ultrasonic treatment for 60 s to ensure uniform dispersion. A small aliquot of the suspension was deposited onto carbon-coated adhesive tabs mounted on aluminum stubs and dried at ambient conditions overnight to allow complete solvent evaporation. The dried specimens were subsequently sputter-coated with a thin layer of gold to improve electrical conductivity and imaged using a field-emission scanning electron microscope (ZEISS Sigma VP, Carl Zeiss AG, Oberkochen, Germany) operated at an accelerating voltage of 10 kV.

SEM coupled with energy-dispersive X-ray spectroscopy (EDS) was further employed to determine the elemental composition and spatial distribution of carbon (C), oxygen (O), and silicon (Si) within the CSNPs. Elemental mapping was conducted to evaluate the dispersion of silica domains within the carbon matrix, providing direct evidence for the formation and structural homogeneity of the carbon–silica hybrid nanoparticles. In addition, SEM was used to directly visualize the interaction between CSNPs and adsorbed nano- and microplastics after adsorption experiments. The surface morphology and attachment behavior of plastic particles on CSNPs were examined to qualitatively assess adsorption coverage, particle–particle interactions, and the role of CSNPs surface features in plastic capture.

2.5.2. Fourier Transform Infrared Spectroscopy

Fourier transform infrared (FTIR) spectra of the CSNPs were collected using a Nicolet iS50 spectrometer (Thermo Fisher Scientific Inc., Waltham, MA, USA). Samples were directly deposited onto the instrument's crystal surface without further preparation. Spectra were recorded in the range of 500–4000 cm^{-1}.

2.5.3. X-Ray Diffraction (XRD)

The crystalline structure and phase composition of LSNPs and CSNPs were analyzed by X-ray diffraction (XRD). Powder XRD patterns were collected using an X-ray diffractometer equipped with Cu Kα radiation (λ = 1.5406 Å) over an appropriate 2 θ range. The diffraction data were used to identify the amorphous or crystalline nature of the samples, assess structural changes induced by carbonization, and evaluate the presence and evolution of silica-related phases in LSNPs and CSNPs.

2.5.4. X-Ray Photoelectron Spectroscopy (XPS)

The surface chemical composition and bonding states of LSNPs and CSNPs were characterized by X-ray photoelectron spectroscopy (XPS). Survey spectra were acquired to determine the elemental composition, while high-resolution spectra of C 1s and Si 2p were collected to analyze the chemical states of carbon and silicon species. The XPS analysis provided insight into surface functional groups, carbon hybridization, and the chemical environment of silica before and after carbonization, enabling evaluation of the formation and surface chemistry of carbon–silica hybrid structures.

2.5.5. Thermogravimetric Analysis (TGA)

Thermal stability and compositional characteristics of LSNPs and CSNPs were examined by thermogravimetric analysis (TGA). The samples were heated from ambient temperature to a designated upper temperature of 900 °C under a controlled atmosphere at a constant heating rate. Weight loss profiles were recorded as a function of temperature to evaluate thermal decomposition behavior, organic and inorganic content, and the effect of carbonization on material stability. TGA data were further used to estimate the relative contributions of carbonaceous and silica components in the hybrid materials.

2.5.6. Brunauer–Emmett–Teller (BET) Surface Area Analysis

The textural properties of LSNPs and CSNPs, including specific surface area and pore structure, were determined by nitrogen adsorption–desorption measurements based on the Brunauer–Emmett–Teller (BET) method. Prior to analysis, samples were degassed under vacuum to remove adsorbed moisture and gases. BET surface area was calculated from adsorption isotherms, while pore size distribution and pore volume were derived. The specific surface area was calculated using the BET equation:

$$\frac{p}{\boldsymbol{\nu}(p_0 - p)} = \frac{1}{\boldsymbol{\nu}_m C} + \frac{C-1}{\boldsymbol{\nu}_m C}\left(\frac{p}{p_0}\right)$$

where p is the equilibrium pressure, p_0 is the saturation pressure, v is the adsorbed gas volume, v_m is the monolayer adsorbed gas volume, and C is the BET constant related to the adsorption energy. The linear plot of p/p_0 versus $1/[v((p_0/p) - 1)]$ in the relative pressure range of 0.05–0.30 was used to determine v_m and C from the slope and intercept. These measurements were employed to assess the impact of carbonization on porosity development and to correlate textural properties with adsorption performance.

2.6. Nano- and Microplastic Adsorption Experiments

Batch adsorption experiments were conducted to evaluate the removal of nano- and microplastics by carbon–silica nanoparticles (CSNPs). Fluorescein isothiocyanate (FITC)-labeled polystyrene particles with nominal diameters of 200, 500, and 1000 nm were used as model contaminants. Adsorption tests were performed under varying initial plastic concentrations, CSNPs dosages, and solution pH values to systematically investigate adsorption behavior. Following adsorption, the residual concentration of plastics in the aqueous phase was quantified using a UV–visible spectrophotometer based on the characteristic absorbance of FITC, while scanning electron microscopy (SEM) was employed to directly visualize the attachment of plastic particles on CSNPs surfaces. Detailed experimental procedures are provided in the Supporting Information.

3. Results and Discussion

3.1. Synthesis Mechanism and Morphology of LSNPs and CSNPs

LSNPs are formed through a pH-triggered co-precipitation and solvent-regulated self-assembly process originating from rice husk black liquor, in which lignin fragments and silicate species coexist in a highly alkaline medium [27]. Under alkaline conditions, lignin exists as deprotonated, amorphous anionic macromolecules with extended and solvated conformations due to strong intramolecular and intermolecular electrostatic repulsion between ionized phenolic and carboxylic groups, while silica is present predominantly as soluble silicate species [28]. This molecularly dispersed state imparts high solution stability while inhibiting particle nucleation [29]. With gradual acidification, lignin is progressively reprotonated, leading to a sharp reduction in solubility and the development of strong intermolecular hydrogen bonding and π–π interactions that drive lignin condensation [30].

Silicate species hydrolyze and condense, precipitating and nucleating silica domains earlier than lignin aggregation at high pH [31]. The simultaneous lignin precipitation and silica condensation promote the nucleation of hybrid lignin–silica clusters, in which lignin preferentially associates with silica interfaces through hydrogen bonding and electrostatic interactions [32]. The introduction of ethanol plays a decisive regulatory role by moderating silica condensation kinetics and reducing interfacial tension, inhibiting uncontrolled lignin self-aggregation and preventing the formation of irregular micron-scale flocs. Instead, lignin molecules reorganize and collapse around the evolving silica-rich nuclei during the aging stage, minimizing surface free energy and generating compact, spherical LSNPs.

The morphology and nanostructure of the resulting LSNPs are revealed by SEM, TEM, and elemental mapping analyses. As shown in Figure 1a, SEM images indicate that LSNPs consist of densely packed, quasi-spherical primary nanoparticles that assemble into a porous three-dimensional particulate framework at the microscale. The primary particles display relatively uniform nanoscale dimensions, while their loose packing generates abundant interparticle voids, indicating a hierarchical aggregation structure rather than a compact, sintered morphology. TEM images (Figure 1b) further reveal that LSNPs possess a nanostructure characterized by electron-dense domains embedded within a lighter continuous matrix. Elemental mapping confirms that carbon and oxygen are broadly distributed throughout the particles, whereas silicon is preferentially localized within the electron-dense regions, indicating the presence of silica-rich nanodomains integrated into a lignin matrix. This spatially heterogeneous elemental distribution suggests that silica is structurally incorporated within the lignin framework instead of forming a separate continuous phase, consistent with the proposed co-precipitation and interfacial assembly mechanism [33]. The resulting hybrid architecture combines silica-rich nanodomains with a continuous lignin phase, yielding structurally integrated lignin–silica nanoparticles with hierarchical porosity and nanoscale compositional heterogeneity.

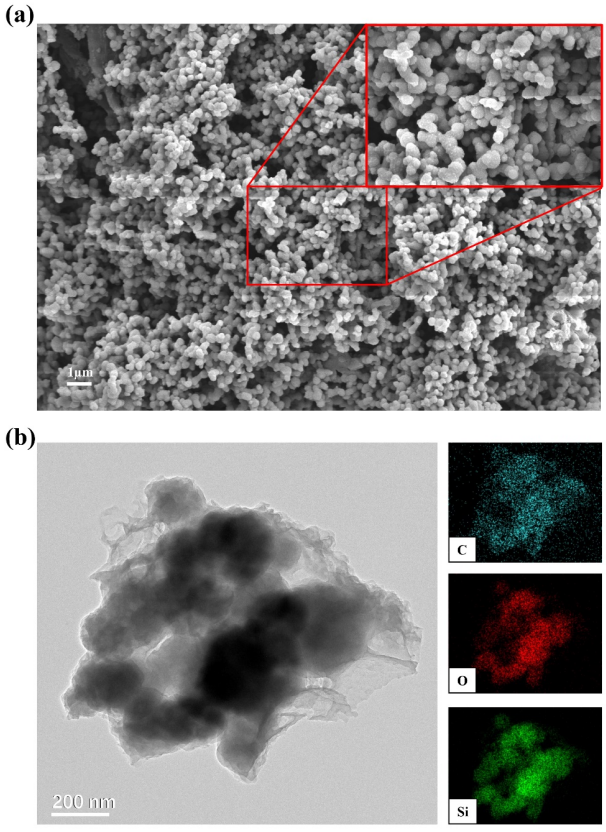


Figure 1. (**a**) SEM images of LSNPs; (**b**) TEM and element mapping photos (C, O, Si) of LSNPs.

3.2. Characterization of LSNPs and CSNPs

The FTIR spectra in Figure 2a illustrate the effects of hybrid particle formation and subsequent carbonization on the chemical structure and functional groups of raw rice husk, the hybrid LSNPs and the carbonized CSNPs. RH exhibits a broad O–H stretching band at ~3432 cm^{-1} (hydrogen-bonded hydroxyl groups from lignocellulosic components and surface silanols), together with an aliphatic –CH3 and –CH2 stretching band at ~2924 cm^{-1} [34]. The band near ~1596 cm^{-1} is assigned to aromatic skeletal vibrations of lignin. In addition, the intense band centered at ~1100 cm^{-1} arises from overlapping C–O stretching vibrations of polysaccharides and asymmetric Si–O–Si stretching of biogenic silica, accompanied by characteristic Si–O bending vibrations at around 800 cm^{-1}. After alkaline extraction and self-assembly, LSNPs retain the characteristic lignin-related aromatic and aliphatic bands, while the Si–O–Si stretching band at ~1108 cm^{-1} becomes more pronounced, confirming the formation of an organic–inorganic hybrid structure. The persistence of a broad O–H band indicates extensive hydrogen bonding between lignin functional groups and silica surfaces. Additional bands at 1460–1270 cm^{-1} are assigned to C–H bending and C–O stretching vibrations associated with syringyl and guaiacyl units [35]. Silica-related features are evident from the intense asymmetric Si–O–Si stretching band at 1108 cm^{-1}, indicating a well-preserved silica framework within the hybrid particles. After thermal carbonization, most lignin-derived hydroxyl and aliphatic C–H vibrations are substantially weakened, reflecting dehydration, dehydrogenation, and side-chain cleavage, whereas a weak band at ~1580–1600 cm^{-1} remains, attributable to conjugated C=C stretching in aromatized carbon domains. The Si–O–Si framework vibrations at ~1100 cm^{-1}, together with the Si–O bending modes, remain well preserved, demonstrating the high thermal stability and effective retention of the silica phase within the carbon–silica hybrid.

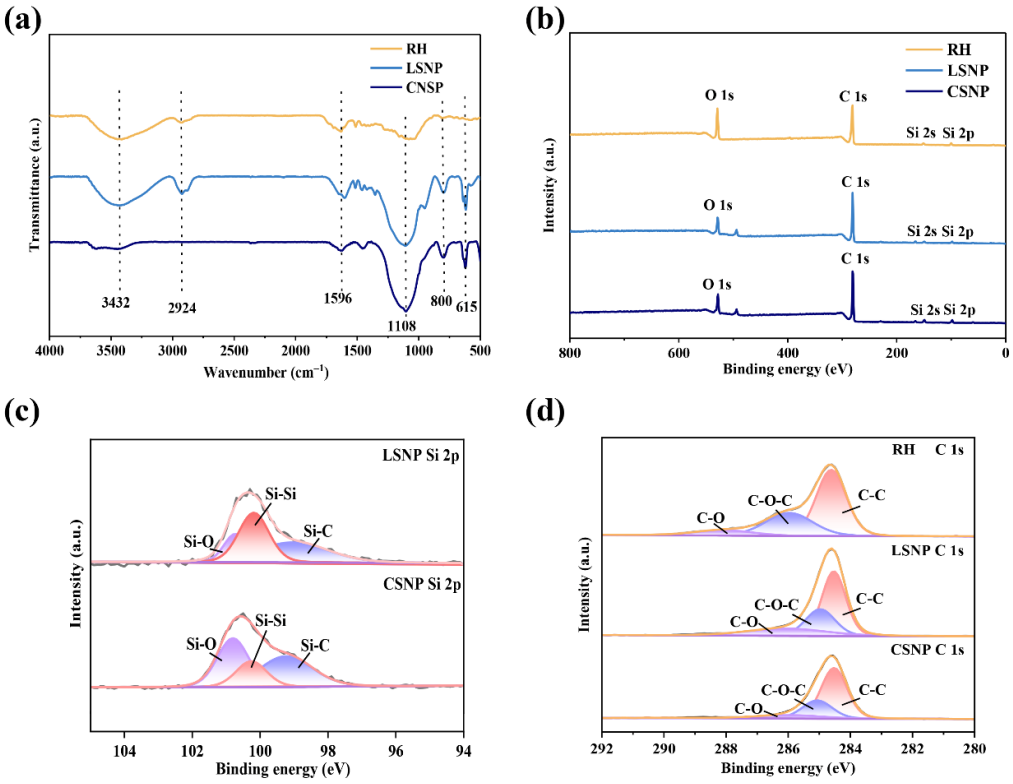


Figure 2. Characterizations of RH, LSNPs and CSNPs. (**a**) FTIR; (**b**) XPS survey spectra; (**c**) XPS Si 2p deconvolution spectra; (**d**) XPS C 1s deconvolution spectra.

XPS analysis further revealed changes in the chemical structure and composition of RH, LSNPs and CSNPs during carbonization. As shown in the survey spectra (Figure 2b), all samples exhibit characteristic C 1s, O 1s, Si 2s and Si 2p signals, confirming the coexistence of organic and inorganic components throughout the transformation process [27]. The enhanced intensity of the C 1s signal of LSNPs indicates effective integration of lignin-derived carbon with the silica framework, forming an organic–inorganic hybrid in which aromatic carbon units are closely associated with silica domains. Following high-temperature carbonization, the increase in C 1s intensity accompanied by a reduction in the O 1s signal indicates progressive deoxygenation and aromatization, while the persistence of the Si 2p peak confirms the thermal stability of the silica phase within the carbonized composite. High-resolution Si 2p XPS spectra of CSNPs (Figure 2c) reveal an increased relative contribution of the Si–C component, accompanied by a subtle downshift of the Si–O–Si peak toward lower binding energy. This observation is indicative of the formation of stronger interfacial Si–C linkages and suggests potential restructuring of the silica network upon high-temperature treatment, which yields a more tightly coupled carbon–silica hybrid interface. Consistently, high-resolution C 1s XPS spectra (Figure 2d) demonstrate a pronounced transformation in carbon bonding configurations. For the RH, multiple oxygenated carbon species including C–O, C–O–C, and C=O functionalities are prominent, reflecting its polysaccharide- and lignin-rich composition. In the LSNPs, these oxygen-containing moieties remain detectable but undergo partial redistribution. After carbonization, the C 1s spectrum of CSNPs is dominated by the C–C/C=C component, while contributions from oxygenated carbon species are substantially reduced, indicating the development of condensed aromatic domains together with the formation of Si–O–C linkages through dehydration condensation of surface Si–OH groups [36].

X-ray diffraction (XRD) patterns provide further insight into progressive structural evolution from raw material to carbonized particles in Figure 3a. The XRD pattern of RH exhibits a broad diffraction halo centered at approximately 2 θ = 20–23°, characteristic of the largely amorphous nature of lignocellulosic biomass arising from the disordered arrangement of cellulose, hemicellulose, and lignin, with only minor contributions from biogenic silica. The LSNPs sample displays a more complex diffraction profile, in which several weak but discernible peaks emerge superimposed on the amorphous background. These features are attributed to the formation of silica-rich domains and partially ordered inorganic–organic hybrid structures. After high-temperature carbonization, the XRD pattern of CSNPs shows a more pronounced broad diffraction band centered at ~24–26°, corresponding to the reflection of turbostratic carbon, indicative of partial aromatization and the development of stacked carbon layers. The absence of sharp graphitic reflections suggests that the carbon framework remains largely disordered. Meanwhile, weak but identifiable silica-related reflections persist, confirming the thermal stability and retention of the silica phase.

TGA results indicate a progressive improvement in thermal stability from RH to LSNPs and CSNPs, consistent with their structural evolution. The RH sample displays a two-stage degradation profile: a minor initial mass loss (~8%) below 150 °C attributed to moisture removal, followed by a major loss of 60.8% between ~200 and 400 °C, corresponding to the thermal degradation of hemicellulose, cellulose, and lignin components. LSNPs exhibit a multistep thermal degradation behavior, beginning with an initial dehydration stage (~2.5%), followed by a broader decomposition region (~15.1%) associated with the breakdown of lignin-derived oxygenated functionalities, and further mass losses of ~23.6% and ~11.9% stable carbonaceous domains at higher temperatures [37]. CSNPs exhibit the highest thermal stability among the three samples, characterized by minimal weight

loss at low temperatures and a gradual mass decrease (~16.4%) at high temperatures, corresponding to the slow decomposition of residual carbonaceous structures.

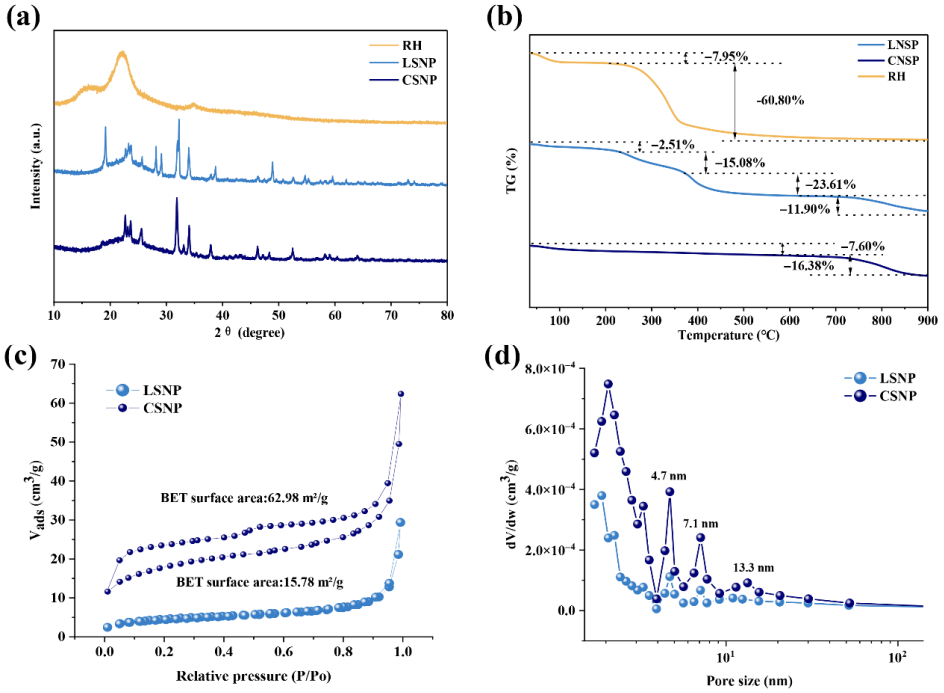


Figure 3. Characterizations of RH, LSNPs and CSNPs. (**a**) XRD; (**b**) TG curves (dashed lines indicate the mass loss percentages at each thermal decomposition stage); (**c**) nitrogen adsorption–desorption isotherms; (**d**) pore size distribution.

Nitrogen adsorption–desorption isotherms reveal a marked evolution in the textural properties upon carbonization. The carbonized CSNP materials possess a substantially greater specific surface area relative to their lignin-rich precursor LSNPs, with BET surface areas of 62.98 m^2 g^{-1} and 15.78 m^2 g^{-1}, respectively. This approximately fourfold enhancement indicates that thermal carbonization generates a significantly larger population of accessible surface sites. In addition, pore volume and average pore size were also determined: LSNPs exhibit a pore volume of 0.019290 cm^3 g^{-1} and an average pore size of 4.89 nm, while CSNPs show a pore volume of 0.053059 cm^3 g^{-1} and an average pore size of 10.99 nm. The increase is attributable to the decomposition of lignin side-chains and elimination of oxygen-containing functionalities, processes that unblock previously inaccessible pores and create new voids within the hybrid matrix. Pore-size distribution analyses further underscore the structural divergence between the materials. Whereas LSNPs exhibit a limited mesoporous contribution, CSNPs display a broadened mesopore distribution, with distinct peaks centered near 4.7, 7.1, and 13.3 nm, signifying the development of a hierarchical pore network during carbonization. The emergence of these mesopores likely results from the contraction and reorganization of lignin-derived carbon in concert with the rigid silica scaffold, which mitigates pore collapse and preserves structural integrity at elevated temperatures. Such hierarchical porosity is particularly favorable for plastic adsorption. The mesoporous hydrophobic carbon surface increases the density of high-energy adsorption sites for nanoscale plastics while facilitating mass transport and the binding of larger plastic particles, which are trapped within the hundreds-of-micrometers hollow pore network of CSNPs. Therefore, the combined increase in accessible surface area and hierarchical mesopore structure promotes more efficient adsorption of plastics spanning a wide size range in CSNPs compared with LSNPs.

3.3. Adsorption Performance of CSNPs Toward Nano- and Microplastics

Adsorption kinetics and the influence of pH on the removal of 500 nm nanoplastics by CSNPs are illustrated in Figure 4. The adsorption capacity exhibits a distinct pH-dependent trend, characterized by maximum uptake under acidic conditions and a gradual decline as the pH shifts toward alkalinity. At low pH, the adsorption behavior is primarily governed by the aggregation and flocculation of CSNPs. These surface charge-mediated processes facilitate the rapid capture of nanoplastics and induce subsequent sedimentation. Under acidic conditions, the protonation of oxygen-containing functional groups (e.g., –OH, $–COO^-$) on the CSNPs surface reduces the negative surface charge, thereby attenuating the electrostatic repulsion between CSNPs and the negatively charged nanoplastics. As a result, CSNPs tend to aggregate into larger clusters, which act as effective flocculants capable of entrapping and sweeping nanoplastic particles from the suspension. This aggregation-induced capture mechanism enhances collision frequency and contact efficiency between CSNPs and nanoplastics, thereby accelerating sedimentation and removal. The kinetic behavior of the system was examined by fitting the experimental data to nonlinear pseudo-first-order and pseudo-second-order models, enabling assessment of the dominant adsorption mechanism.

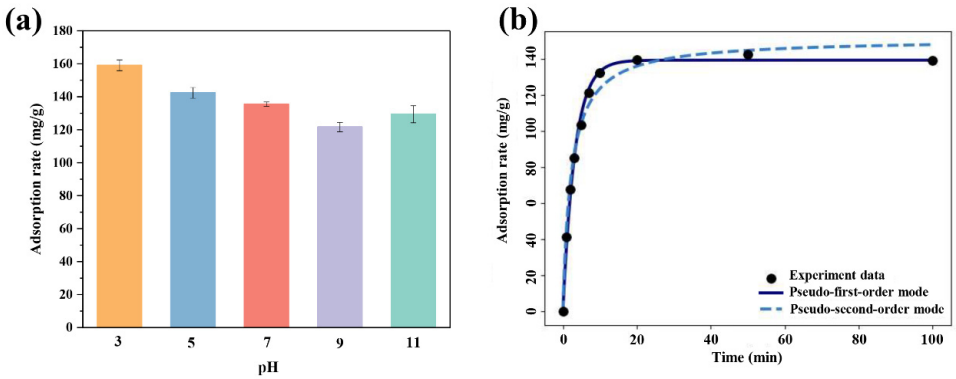


Figure 4. (**a**) Effects of pH on the adsorption of 500 nm nanoplastic; (**b**) adsorption kinetics of CSNPs for nanoplastic removal.

The adsorption kinetics (Figure 4b) reveal a rapid initial uptake stage followed by a slower approach to equilibrium, consistent with a surface-controlled adsorption process. Based on the kinetic fitting results, the adsorption behavior of nanoplastics onto CSNPs is better described by the pseudo-first-order kinetic model, as evidenced by its higher correlation coefficient (R^2) compared with the pseudo-second-order model. This statistical fitting indicates that the adsorption process is governed primarily by physisorption and diffusion-controlled mechanisms rather than chemisorption. The close correspondence between experimental and fitted data suggests that the nanoplastic uptake rate is governed principally by the availability of accessible active sites and physical interfacial interactions. The rapid establishment of equilibrium reflects efficient mass transfer and interfacial contact, characteristics attributed to the porous architecture and high surface accessibility of the carbon–silica composite. These findings confirm that nanoplastic capture by CSNPs is driven by surface-controlled adsorption rather than slow diffusion-limited or reaction-limited mechanisms.

While the present study focuses on adsorption kinetics, a comprehensive understanding of the adsorption equilibrium and diffusion mechanisms would require further investigation. Isotherm modeling and intraparticle diffusion analysis are planned for future work to elucidate the thermodynamic driving forces and rate-controlling steps governing nanoplastic capture by CSNPs.

Variations in nanoplastic size, concentration, and biochar dosage critically influence the adsorption performance of CSNPs (Figure 5), thereby elucidating the dominant mechanisms regulating particle–surface interactions. At a fixed CSNPs dosage, increasing the initial nanoplastic concentration from 0.25 to 2 mg mL^{-1} resulted in a systematic rise in adsorption capacity for all particle sizes. This trend is attributed to the stronger mass-transfer driving force at higher concentrations, which facilitates the occupation of active sites on the CSNPs surface. Among the sizes investigated, 500 nm particles consistently exhibited the highest capacity, surpassing both 200 nm and 1000 nm variants. This suggests that intermediate-sized nanoplastics achieve an optimal balance between specific surface area and collision efficiency. Conversely, the uptake of 200 nm particles appears limited by Brownian motion and electrostatic stabilization, which hinder attachment despite the particles' high surface-area-to-volume ratio. The 1000 nm particles are similarly constrained, though primarily by their lower specific surface area and reduced interfacial contact efficiency. A consistent size-dependent pattern emerged when varying the CSNPs dosage. Increasing the dosage from 2 to 20 mg mL^{-1} enhanced nanoplastic removal across all sizes by providing more active binding sites; however, the capacity gains were non-linear at higher loadings. This plateauing effect implies that CSNPs' self-aggregation and site overlap reduce the effective surface area accessible for binding. In total, 500 nm particles displayed the most pronounced response to increased dosage, whereas the gains for 200 nm and 1000 nm particles were more gradual, reinforcing the limiting roles of colloidal stability and steric constraints, respectively. These findings elucidate a size-selective adsorption mechanism governed by the interplay of surface availability and interfacial dynamics. The superior performance of intermediate-sized particles underscores the importance of particle-scale matching between adsorbent and pollutant, indicating that operating conditions must be optimized to maximize removal efficiency across heterogeneous nanoplastic populations. The better adsorption performance toward 500 nm nanoplastics highlights the importance of particle-scale matching between adsorbent and pollutant, and suggests that optimizing CSNPs dosage and operating conditions is critical for maximizing removal efficiency across heterogeneous nanoplastic populations in aquatic environments.

Compared with conventional adsorbents such as activated carbon and zeolites, the CSNPs developed in this work offer distinct advantages. While activated carbon typically exhibits high adsorption capacity for organic pollutants, its production relies on non-renewable precursors and involves energy-intensive activation processes. Zeolites and metal oxides, though effective for certain contaminants, often suffer from limited affinity toward hydrophobic plastic particles. In contrast, the carbon–silica hybrid structure of CSNPs combines the hydrophobic affinity of carbon domains with the structural stability of silica, enabling effective capture of both nano- and microplastics. Furthermore, the use of rice husk black liquor—an underutilized agricultural byproduct—as the sole precursor provides a sustainable and cost-effective alternative to synthetic adsorbents. A quantitative comparison of adsorption capacities is not directly feasible due to differences in experimental conditions and target contaminants across studies, but the present work demonstrates that CSNPs represent a promising bio-based adsorbent for broad-spectrum plastic removal.

3.4. Nano- and Microplastic Mechanism

The SEM micrographs presented in Figure 6 provide compelling visual evidence of the size-dependent capture of nanoplastics and microplastics by CSNPs. These images reveal that the material employs distinct adsorption and immobilization mechanisms that transition systematically across particle size domains. In the case of 200 nm nanoplastics, a significant population of spherical particles is observed to be preferentially sequestered within the nanoscale voids, interstices, and surface cavities inherent to the CSNP matrix.

This behavior indicates that the adsorption process is predominantly governed by pore filling and intimate surface contact. The material's high specific surface area, combined with its abundant nanoscale roughness, generates a multitude of high-energy adsorption sites. These sites facilitate robust particle–surface interactions, thereby enabling the efficient immobilization of smaller nanoplastics within the internal structure.

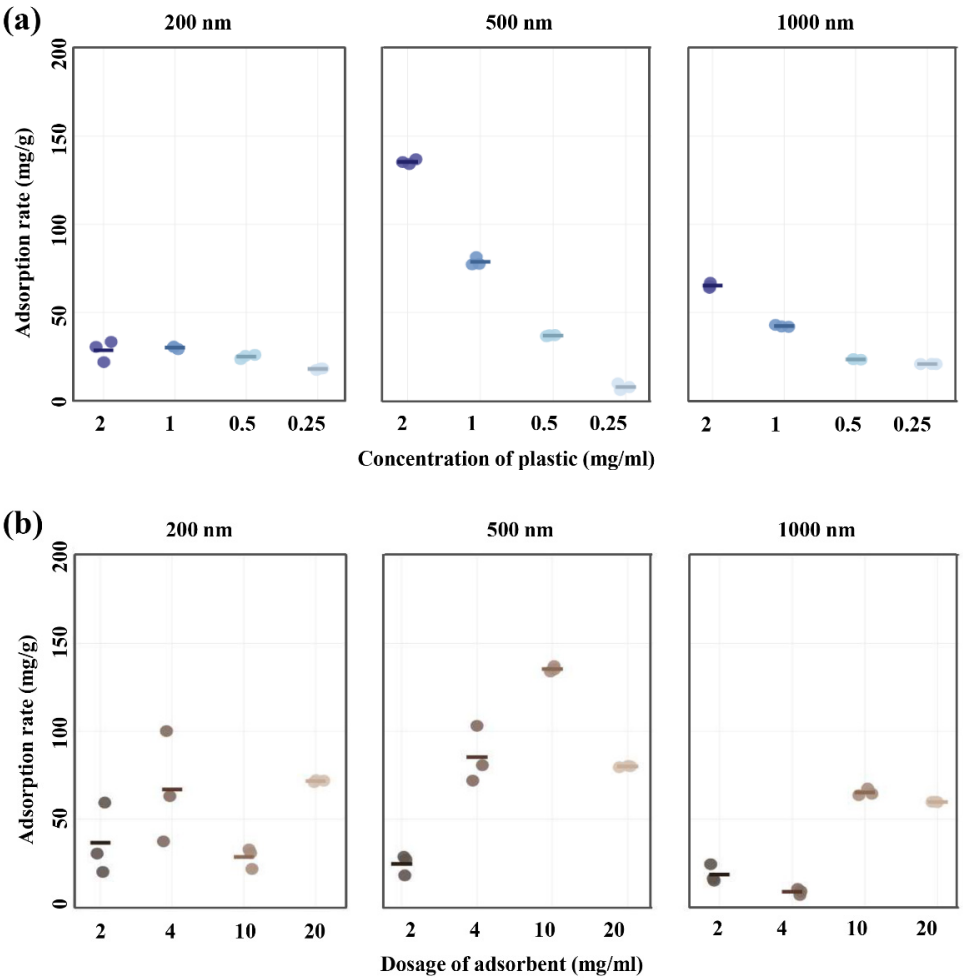


Figure 5. (**a**) Effect of plastic particle concentrations at 10 mg/mL dosage; (**b**) CSNPs adsorbent addition effect at 2 mg mL^{-1} plastic concentration for nano- and microplastic (200 nm, 500 nm, 1000 nm) removal.

As the target particle size increases to 500 nm, a transitional behavior emerges. The nanoplastics are no longer confined exclusively within nanoscale pores; instead, they are observed to be partially embedded within larger mesoscopic depressions while simultaneously adhering to the external CSNPs surfaces. This intermediate regime is characteristic of a mixed adsorption mechanism that synergistically combines surface attachment with partial physical entrapment. Here, hydrophobic interactions between the plastic surface and the carbon-rich domains of the CSNPs act as the dominant driving force. Furthermore, the rough, hierarchical surface morphology of the CSNPs promotes multipoint contact, which significantly enhances adhesion stability even for these larger particulates. For 1000 nm microplastics, direct pore filling becomes sterically unfavorable due to size exclusion effects. Therefore, the adsorption mechanism is dominated by the physical encapsulation of large biochar fragments, wherein CSNPs aggregates effectively surround and physically capture the plastic particles. In this scenario, the hydrophobic carbon framework facilitates a strong chemical affinity toward the plastic surface, while interparticle aggregation results

in effective envelopment and co-transport. Collectively, these observations demonstrate that CSNPs exhibit a highly versatile, size-adaptive adsorption behavior: nanoscale plastics are immobilized via pore-filling and surface adsorption, whereas larger microplastics are removed through aggregate-assisted encapsulation. This multi-scale capture capability highlights the exceptional effectiveness of carbon–silica hybrids for broad-spectrum plastic removal from nano- to microscale dimensions.

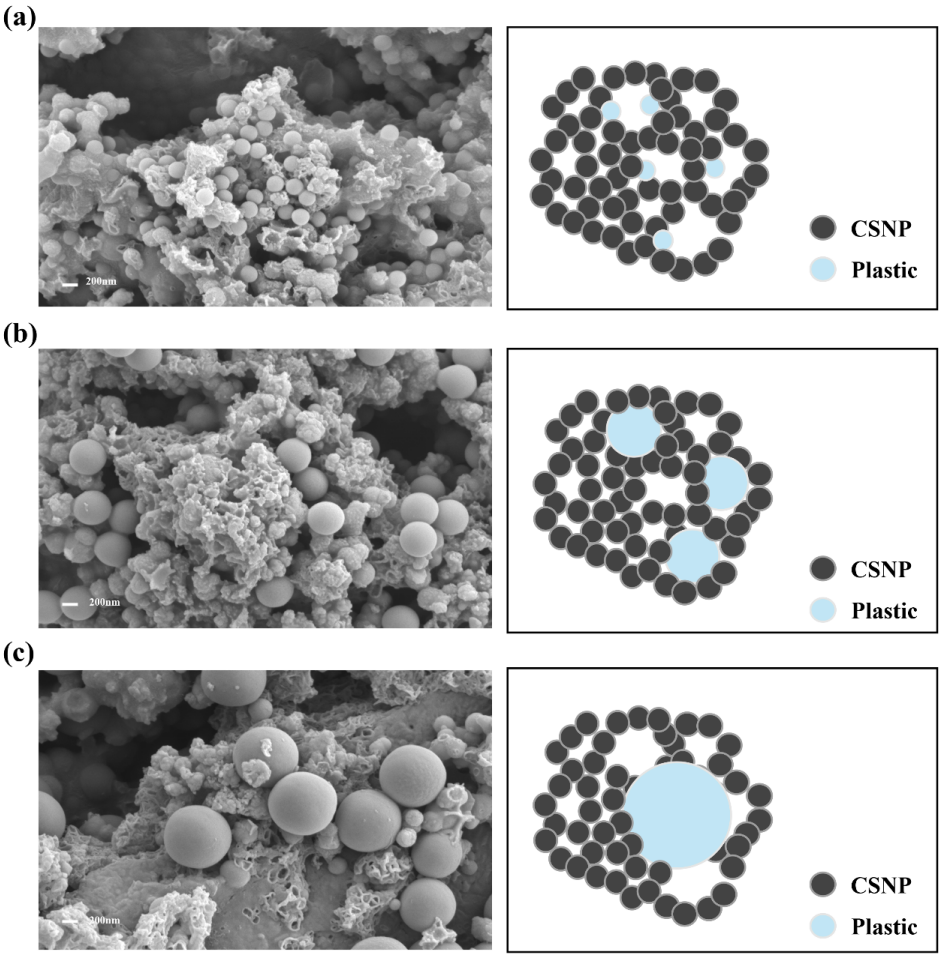


Figure 6. CNSP adsorption mechanism illustrated by SEM images for (**a**) 200 nm; (**b**) 500 nm; (**c**) 1000 nm.

4. Conclusions

Sustainable and waste-recycling biorefinery strategies were developed to synthesize CSNPs from rice husk-derived black liquor via controlled lignin–silica self-assembly followed by thermal carbonization. Comprehensive structural and surface characterizations confirmed that carbonization transforms lignin–silica nanoparticles into a hierarchically porous, thermally stable carbon–silica hybrid featuring enhanced aromaticity, reduced oxygen functionality, and strengthened interfacial coupling between carbon and silica domains. The resulting CSNPs exhibit significantly increased specific surface area and a well-developed mesoporous network, which together provide abundant and accessible adsorption sites. Batch adsorption experiments demonstrate that CSNPs enable rapid and efficient removal of nano- and microplastics across a wide size range, with optimal performance observed for intermediate-sized (500 nm) nanoplastics. Adsorption kinetics are best described by a pseudo-first-order model, indicating that plastic capture is governed primarily by surface-controlled physisorption and diffusion-driven interactions rather than chemisorption-limited processes. SEM observations further reveal a size-adaptive capture

mechanism, in which small nanoplastics are immobilized through pore filling and surface adsorption, while larger microplastics are removed via aggregate-assisted encapsulation and physical entrapment. From a sustainability perspective, the synthesis route utilizes rice husk black liquor—an underutilized agricultural byproduct—as the sole precursor, aligning with circular economy principles. The relatively simple self-assembly and carbonization procedure also suggests potential for scalable production with minimal reliance on external reagents. Despite these promising results, several limitations should be acknowledged with respect to real-world applicability, sustainability, and long-term reusability. The adsorption experiments were conducted under controlled laboratory conditions using model polystyrene particles in simplified matrices. While this approach allows for a fundamental understanding of the adsorption mechanisms, natural aquatic environments are far more complex. They typically contain dissolved organic matter (e.g., humic substances), natural colloids, and varying ionic strengths, all of which may influence the adsorption behavior of CSNPs through competition, shielding, or aggregation effects. Therefore, the performance of CSNPs in complex natural waters containing these competing components remains to be evaluated. In addition, the current synthesis and adsorption assessments were performed at laboratory scale, and further optimization of material yield, energy input during carbonization, and process economics is required to assess large-scale feasibility. Future work should therefore focus on several key directions: (i) scaling up production and improving carbon yield and energy efficiency; (ii) evaluating the adsorption performance of CSNPs in simulated environmental water matrices or real water samples to account for the effects of dissolved organic matter and ionic strength; (iii) investigating the regeneration and reuse performance of the adsorbent to assess its long-term applicability; and (iv) exploring the potential for recovering and reusing the adsorbed plastics. Based on the thermal and chemical stability of the carbon–silica hybrid structure, thermal regeneration or solvent washing may be feasible for adsorbent reuse, though systematic studies are needed to evaluate regeneration efficiency and cycling stability. Addressing these aspects will provide a more comprehensive assessment of the material's efficacy under realistic conditions and facilitate its potential translation to field applications. CSNPs represent a versatile, low-cost adsorbent capable of broad-spectrum plastic removal, while offering an effective pathway for the high-value valorization of black liquor and rice husk biomass in advanced water purification applications.

Supplementary Materials: The following supporting information can be downloaded at: https://www.mdpi.com/article/10.3390/su18083721/s1, Figure S1: SEM and element mapping of LSNPs; Figure S2: SEM and element mapping of CSNPs; Table S1: Adsorption kinetics of 500 nm plastic particles by CSNP; Table S2: The cost–benefit analysis for the adsorbent.

Author Contributions: Conceptualization, W.G.; Methodology, Q.L.; Validation, Q.L.; Formal analysis, W.G.; Investigation, W.G.; Resources, X.C.; Writing—original draft, W.G.; Writing—review & editing, Q.L. and D.Z.; Supervision, Q.L., D.Z. and X.C.; Project administration, X.C.; Funding acquisition, X.C. All authors have read and agreed to the published version of the manuscript.

Funding: This research was funded by National Natural Science Foundation of China grant number 52539005; 52479064; 52209088; Guangzhou Institute of Science and Technology, grant number SL2024A04J00638; Basic and Applied Basic Research Foundation of Guangdong Province, grant number 2024A1515011047; 2025A1515011022.

Institutional Review Board Statement: Not applicable.

Informed Consent Statement: Not applicable.

Data Availability Statement: The original contributions presented in this study are included in the article/Supplementary Materials. Further inquiries can be directed to the corresponding author.

Acknowledgments: The authors would like to acknowledge the financial and technical support from South China University of Technology.

Conflicts of Interest: The authors declare no conflict of interest.

References

1. Akhtar, N.; Syakir Ishak, M.I.; Bhawani, S.A.; Umar, K. Various natural and anthropogenic factors responsible for water quality degradation: A review. *Water* **2021**, *13*, 2660. [CrossRef]
2. Swaminaathan, P.; Thamarai, P.; Yaashikaa, P.; Saravanan, A.; Vickram, A. Microbial bioremediation of dyes, metals, and microplastics for ecological sustainability. *Energy Ecol. Environ.* **2025**, *10*, 45–65. [CrossRef]
3. Borrelle, S.B.; Ringma, J.; Law, K.L.; Monnahan, C.C.; Lebreton, L.; McGivern, A.; Murphy, E.; Jambeck, J.; Leonard, G.H.; Hilleary, M.A.; et al. Predicted growth in plastic waste exceeds efforts to mitigate plastic pollution. *Science* **2020**, *369*, 1515–1518. [CrossRef] [PubMed]
4. Hirt, N.; Body-Malapel, M. Immunotoxicity and intestinal effects of nano- and microplastics: A review of the literature. *Part. Fibre Toxicol.* **2020**, *17*, 57. [CrossRef] [PubMed]
5. Na, S.H.; Kim, M.J.; Kim, J.T.; Jeong, S.; Lee, S.; Chung, J.; Kim, E.J. Microplastic removal in conventional drinking water treatment processes: Performance, mechanism, and potential risk. *Water Res.* **2021**, *202*, 117417. [CrossRef] [PubMed]
6. Cordier, M.; Uehara, T.; Jorgensen, B.; Baztan, J. Reducing plastic production: Economic loss or environmental gain? *Camb. Prism. Plast.* **2024**, *2*, e2. [CrossRef]
7. Xia, C.; Cai, L.; Lam, S.S.; Sonne, C. Microplastics pollution: Economic loss and actions needed. *Eco-Environ. Health* **2023**, *2*, 41–42. [CrossRef]
8. Liang, R.; Hu, A.; Hatat-Fraile, M.; Zhou, N. Fundamentals on adsorption, membrane filtration, and advanced oxidation processes for water treatment. In *Nanotechnology for Water Treatment and Purification*; Springer: Berlin/Heidelberg, Germany, 2014; pp. 1–45.
9. Akhtar, M.S.; Ali, S.; Zaman, W. Innovative Adsorbents for Pollutant Removal: Exploring the Latest Research and Applications. *Molecules* **2024**, *29*, 4317. [CrossRef]
10. Gu, W.; Yushin, G. Review of nanostructured carbon materials for electrochemical capacitor applications: Advantages and limitations of activated carbon, carbide-derived carbon, zeolite-templated carbon, carbon aerogels, carbon nanotubes, onion-like carbon, and graphene. *Wiley Interdiscip. Rev. Energy Environ.* **2014**, *3*, 424–473. [CrossRef]
11. Jaria, G.; Calisto, V.; Esteves, V.I.; Otero, M. Overview of relevant economic and environmental aspects of waste-based activated carbons aimed at adsorptive water treatments. *J. Clean. Prod.* **2022**, *344*, 130984. [CrossRef]
12. Jjagwe, J.; Olupot, P.W.; Menya, E.; Kalibbala, H.M. Synthesis and application of granular activated carbon from biomass waste materials for water treatment: A review. *J. Bioresour. Bioprod.* **2021**, *6*, 292–322. [CrossRef]
13. Sagadevan, S.; Fatimah, I.; Mathanmohun, M.; Lett, J.A.; Al-Anber, M.A. Biowaste-derived carbon for wastewater treatment: A sustainable and cost-effective approach. *Biomass Convers. Biorefinery* **2025**, *15*, 13323–13345. [CrossRef]
14. Liou, T.-H.; Wang, S.-Y.; Lin, Y.-T.; Yang, S. Sustainable utilization of rice husk waste for preparation of ordered nanostructured mesoporous silica and mesoporous carbon: Characterization and adsorption performance. *Colloids Surf. A Physicochem. Eng. Asp.* **2022**, *636*, 128150. [CrossRef]
15. Xiong, W.; Yang, D.; Alam, M.A.; Xu, J.; Li, Y.; Wang, H.; Qiu, X. Structural regulation of lignin/silica nanocomposites by altering the content of quaternary ammonium groups grafted into softwood kraft lignin. *Ind. Crops Prod.* **2020**, *144*, 112039. [CrossRef]
16. Marcuello, C.; Bercu, N.; Foulon, L.; Chabbert, B.; Molinari, M.; Aguié-Béghin, V. Impact of lignin structuration on its chemical and adhesive properties at the nanoscale: Involvement with native and polymer matrices. *Nanoscale* **2025**, *17*, 24657–24668. [CrossRef]
17. Sethupathy, S.; Murillo Morales, G.; Gao, L.; Wang, H.; Yang, B.; Jiang, J.; Sun, J.; Zhu, D. Lignin valorization: Status, challenges and opportunities. *Bioresour. Technol.* **2022**, *347*, 126696. [CrossRef]
18. Bajwa, D.S.; Pourhashem, G.; Ullah, A.H.; Bajwa, S.G. A concise review of current lignin production, applications, products and their environmental impact. *Ind. Crops Prod.* **2019**, *139*, 111526. [CrossRef]
19. Lim, H.Y.; Yusup, S.; Loy, A.C.M.; Samsuri, S.; Ho, S.S.K.; Manaf, A.S.A.; Lam, S.S.; Chin, B.L.F.; Acda, M.N.; Unrean, P. Review on conversion of lignin waste into value-added resources in tropical countries. *Waste Biomass Valoriz.* **2021**, *12*, 5285–5302. [CrossRef]
20. Sharma, S.K.; Sharma, G.; Sharma, A.; Bhardwaj, K.; Preeti, K.; Singh, K.; Kumar, A.; Pal, V.K.; Choi, E.H.; Singh, S.P. Synthesis of silica and carbon-based nanomaterials from rice husk ash by ambient fiery and furnace sweltering using a chemical method. *Appl. Surf. Sci. Adv.* **2022**, *8*, 100225. [CrossRef]
21. Al-Amsyar, S.M. Sulfonated-silica/carbon composites from rice husk as heterogeneous catalysts in fructose conversion: The effect of controlling carbonization temperature of rice husk on its physicochemical properties and catalytic activities. *Microporous Mesoporous Mater.* **2022**, *336*, 111896. [CrossRef]

22. Steiger, B.G.; Zhou, Z.; Anisimov, Y.A.; Evitts, R.W.; Wilson, L.D. Valorization of agro-waste biomass as composite adsorbents for sustainable wastewater treatment. *Ind. Crops Prod.* **2023**, *191*, 115913. [CrossRef]
23. Tan, X.-F.; Zhu, S.-S.; Wang, R.-P.; Chen, Y.-D.; Show, P.-L.; Zhang, F.-F.; Ho, S.-H. Role of biochar surface characteristics in the adsorption of aromatic compounds: Pore structure and functional groups. *Chin. Chem. Lett.* **2021**, *32*, 2939–2946. [CrossRef]
24. Patwardhan, S.V.; Emami, F.S.; Berry, R.J.; Jones, S.E.; Naik, R.R.; Deschaume, O.; Heinz, H.; Perry, C.C. Chemistry of aqueous silica nanoparticle surfaces and the mechanism of selective peptide adsorption. *J. Am. Chem. Soc.* **2012**, *134*, 6244–6256. [CrossRef] [PubMed]
25. Wu, T.; Ke, Q.; Lu, M.; Pan, P.; Zhou, Y.; Gu, Z.; Cui, G.; Lu, H. Recent advances in carbon-silica composites: Preparation, properties, and applications. *Catalysts* **2022**, *12*, 573. [CrossRef]
26. Ling, Q.; Harrison, M.D.; Hassanpour, M.; Zhang, Z. Rice husk derived lignin/silica hybrid nanoparticles stabilized Pickering emulsion for phytosterol ester biosynthesis. *Int. J. Biol. Macromol.* **2024**, *283*, 37600. [CrossRef]
27. Jiang, C.; Shen, H.; Bi, X.; Wang, Z.; Yao, M.; Wu, Y.; Zhang, L.; Yu, P. A green dual-phase carbon-silica nanohybrid derived from black liquor lignin for reinforcing styrene-butadiene rubber. *Compos. Sci. Technol.* **2022**, *230*, 109775. [CrossRef]
28. Budnyak, T.M.; Pylypchuk, I.V.; Lindström, M.E.; Sevastyanova, O. Electrostatic deposition of the oxidized kraft lignin onto the surface of aminosilicas: Thermal and structural characteristics of hybrid materials. *ACS Omega* **2019**, *4*, 22530–22539. [CrossRef]
29. Zwilling, J.D.; Jiang, X.; Zambrano, F.; Venditti, R.A.; Jameel, H.; Velev, O.D.; Rojas, O.J.; Gonzalez, R. Understanding lignin micro-and nanoparticle nucleation and growth in aqueous suspensions by solvent fractionation. *Green Chem.* **2021**, *23*, 1001–1012. [CrossRef]
30. Xia, Q.; Liu, Y.; Meng, J.; Cheng, W.; Chen, W.; Liu, S.; Liu, Y.; Li, J.; Yu, H. Multiple hydrogen bond coordination in three-constituent deep eutectic solvents enhances lignin fractionation from biomass. *Green Chem.* **2018**, *20*, 2711–2721. [CrossRef]
31. Xiong, W.; Yang, D.; Zhong, R.; Li, Y.; Zhou, H.; Qiu, X. Preparation of lignin-based silica composite submicron particles from alkali lignin and sodium silicate in aqueous solution using a direct precipitation method. *Ind. Crops Prod.* **2015**, *74*, 285–292. [CrossRef]
32. Liu, X.; Liu, Q.; Wang, S.; Liu, Z.; Yang, G.; Wang, H.; Xiong, W.; Li, P.; Xu, F.; Xi, Y. Effect of functional group and structure on hydrophobic properties of environment-friendly lignin-based composite coatings. *Int. J. Biol. Macromol.* **2022**, *215*, 132–140. [CrossRef]
33. Xue, B.; Wang, X.; Yu, L.; Di, B.; Chen, Z.; Zhu, Y.; Liu, X. Self-assembled lignin-silica hybrid material derived from rice husks as the sustainable reinforcing fillers for natural rubber. *Int. J. Biol. Macromol.* **2020**, *145*, 410–416. [CrossRef]
34. Shi, Z.; Xu, G.; Deng, J.; Dong, M.; Murugadoss, V.; Liu, C.; Shao, Q.; Wu, S.; Guo, Z. Structural characterization of lignin from D. sinicus by FTIR and NMR techniques. *Green Chem. Lett. Rev.* **2019**, *12*, 235–243. [CrossRef]
35. Zhang, H.; Ding, X.; Chen, X.; Ma, Y.; Wang, Z.; Zhao, X. A new method of utilizing rice husk: Consecutively preparing d-xylose, organosolv lignin, ethanol and amorphous superfine silica. *J. Hazard. Mater.* **2015**, *291*, 65–73. [CrossRef]
36. Zhong, Y.; Qiu, X.; Gao, J.; Guo, Z. Chemical structure of Si–O in silica fume from ferrosilicon production and its reactivity in alkali dissolution. *ISIJ Int.* **2019**, *59*, 1098–1104. [CrossRef]
37. Vecchio Ciprioti, S.; Catauro, M.; Bollino, F.; Tuffi, R. Thermal behavior and dehydration kinetic study of SiO_2/PEG hybrid gel glasses. *Polym. Eng. Sci.* **2017**, *57*, 606–612. [CrossRef]

Disclaimer/Publisher's Note: The statements, opinions and data contained in all publications are solely those of the individual author(s) and contributor(s) and not of MDPI and/or the editor(s). MDPI and/or the editor(s) disclaim responsibility for any injury to people or property resulting from any ideas, methods, instructions or products referred to in the content.